

From molecules to solids with the DMol³ approach

B. Delley

Paul Scherrer Institut, WHGA/123, CH-5232 Villigen PSI, Switzerland

(Received 6 June 2000; accepted 17 August 2000)

Recent extensions of the DMol³ local orbital density functional method for band structure calculations of insulating and metallic solids are described. Furthermore the method for calculating semilocal pseudopotential matrix elements and basis functions are detailed together with other unpublished parts of the methodology pertaining to gradient functionals and local orbital basis sets. The method is applied to calculations of the enthalpy of formation of a set of molecules and solids. We find that the present numerical localized basis sets yield improved results as compared to previous results for the same functionals. Enthalpies for the formation of H, N, O, F, Cl, and C, Si, S atoms from the thermodynamic reference states are calculated at the same level of theory. It is found that the performance in predicting molecular enthalpies of formation is markedly improved for the Perdew–Burke–Ernzerhof [Phys. Rev. Lett. **77**, 3865 (1996)] functional. © 2000 American Institute of Physics. [S0021-9606(00)30342-7]

INTRODUCTION

This article describes the local orbital density functional (DF) method DMol³ which evolved from a gas phase molecular method to a method, which with its recent advances, encompasses possibilities for state of the art calculations on insulating and metallic solids. In this article, solid state calculations are applied to the calculation of enthalpies of atom formation for the elements C, Si, and S from their thermodynamic reference states.

On the methodological side, the step from finite molecules and clusters to solids involves the necessity of dealing appropriately with the infinite number of eigenstates of the solid. This is done as usual, by idealizing to solid for perfect translation symmetry with respect to a unit cell. The symmetry representations for the lattice translations require a continuum of labels, the vectors in reciprocal space inside the first Brillouin zone. The molecular sum over orbitals generalizes into an integration over the first Brillouin zone (BZ).

The basic description of the DMol method for molecules can be found in Ref. 1. The localized numerical orbitals used as basis sets are designed to give a maximum of accuracy for a given basis set size.¹ This is done by treating the separated atom limit exactly with the numerical atomic basis functions. The atomic response to the molecular or solid environment can be handled robustly to an excellent approximation by a relatively small number of additional numerical functions.¹ With the increase of compute power available, a regime has been reached where the localized basis sets can be implemented with linear scaling algorithms. This perspective has been addressed by introducing basis functions with a strictly finite range. The pertinent details are given in the subsection on short tail localized basis functions below. The generalization of the method to calculate the static potential for periodic boundary conditions in a bulk system has been described in Ref. 2. In order to stabilize the total energy and the atomic dissociation energy on approaching self-consistency, a Harris functional form is used.^{3,4,1} Contrary to the usual

applications of the Harris functional which use nonself-consistent simple forms of the density, DMol is normally run to give accurate self-consistent field (SCF) densities. It is possible, however, to use it for non-SCF Harris calculations, but the rest of this article is not concerned with this. Liquids and molecules in solution are examples of extended systems without the translational symmetry of crystals. This can be addressed in an approximate way within the conductor screening model of Klamt.⁵ The DMol method relies fully on numerical integration in 3D for all matrix elements. Numerical integrations in 3D are also used at some point for calculating DF correlation matrix elements by all other current DF methods. Projections as well as all space integrations involve numerical integrations on a sphere. This subject has been discussed in more detail in Ref. 6. A generalization of the method to include scalar relativistic effects via a local pseudopotential for all electron calculations has been given in Ref. 7. More flexibility and suppression of core states can be obtained with semilocal pseudopotentials. In a subsection below, details are given about the implementation of such semilocal pseudopotentials in DMol³.

Extended systems with translational symmetry, crystalline solids, can be treated without further approximations beyond the density functional approximation, provided the translational symmetry group is used. The representations of this group are conveniently labeled by wave vectors. The wave vectors are vectors with dimensions [length⁻¹], hence the notion reciprocal space. Very often, however, the reciprocal space representation vectors are expressed as dimensionless fractions of the reciprocal lattice vectors. The notion *k*-points is frequently used for wave vectors.

A subsection of this article describes the generalization of the DMol method to use arbitrary reciprocal space representations needed for accurate summation over occupied orbitals, etc., in crystals. This now allows proper calculations for smaller unit cells where band dispersion across the first Brillouin zone makes the Γ -point approximation inappropriate.

The method for solids is applied to calculate the cohesion and zero-point vibrations for the thermodynamic reference states for graphite, Si, and α -S₈.

NEW METHOD FEATURES

Localized basis functions

Localized basis functions almost automatically lead to sparse one-electron Hamiltonian matrices for large systems. It is useful to review briefly some basic alternatives on how the finite range can be exploited in computations. With the commonly used Gaussian basis sets, usually a truncation threshold is set and matrix elements below that threshold are approximated as exactly zero. Outside some radius this basis is dominated by a single Gaussian. The actual truncation radius at a given threshold can be reduced by raising the exponent of the Gaussian and thus reducing its range. If one desires to push the cutoff radius down as much as possible, at a given radius one has to optimize accuracy by balancing the adverse effects of reducing the range of the outermost Gaussian against the error from raising the truncation threshold. Raising the truncation threshold implies a discontinuity of the matrix element as a function of distance.

Another possibility is to use numerical atomic functions and enforce a zero boundary condition at some radius. This procedure implies a discontinuity of the derivative of the radial function at the cutoff. The treatment of the second derivative needed for the kinetic energy requires special care. Sankey and Niklevski⁸ chose to treat the kinetic energy term in reciprocal space. Comparing the two methods it appears that the tails of a Gaussian basis are similar to ones obtained from an atomic confinement by a harmonic potential, while the other method uses a hard wall confinement.

In the present method, advantages of the two other methods are combined. A soft confining potential similar to the harmonic potential minimizes the effect of any discontinuity at the cutoff, and allows calculation of the kinetic energy part in real space. A hard wall boundary condition at the cutoff radius puts the lowest discontinuity to the first derivative as in the second method. Since the present method uses basis functions from numerical atoms or more general central field systems, there is freedom to replace the harmonic potential by a higher power of the radius, and thus to extend the radial range where the basis functions closely follow the atomic exponential behavior. As the method moves toward smaller cutoff radii, this soft confining potential will need to be optimized.

Semilocal pseudopotential matrix elements

Main motivations for the use of pseudopotentials come from systems with heavy atoms. The pseudopotential allows to incorporate relativistic effects which can be described by scalar wave functions in a nonrelativistic framework. The reduction of the number of basis functions helps to speed up calculation of the Hamiltonian matrix and diagonalization. Semilocal pseudopotentials are usually decomposed as

$$V_{\text{ps}}(\mathbf{r}, \mathbf{r}') = V_{\text{loc}}(r) + \sum_{lm} |lm\rangle V_l(r) \langle lm|, \quad (1)$$

into a local part V_{loc} and a nonlocal part where the potential V_l acts only on the partial waves with angular momentum l . By calculating the projections numerically on the angular subsets of points associated with each atom,

$$A_{l,m,\alpha,j} = \int Y_{lm}(\mathbf{r} - \mathbf{r}_\alpha) \phi_j(\mathbf{r}) d\Omega, \quad |\mathbf{r} - \mathbf{r}_\alpha| < \tau_{\text{nonlocal}}, \quad (2)$$

it is found that the use of the separable pseudopotentials $V_{\text{ps}}(\mathbf{r}, \mathbf{r}') - V_{\text{loc}}(r) = \sum_{lm} |\zeta_{lm}\rangle f_l(\zeta_{lm}) \langle \zeta_{lm}|$ (Refs. 9, 10) would not significantly accelerate the evaluation of the pseudopotential matrix elements. The pseudopotential matrix setup time is dominated by Eq. (2). Exactly the same number and type of terms would have to be summed up for a single separable projector. The compute time spent with pseudopotential matrix elements in the present implementation usually remains a small part of the total time spent on matrix elements.

At the present stage, effective core potentials (ECP) of the Stuttgart–Dresden^{11,12} group, which have been derived in the context of wave function approaches, have been adapted for the use with DMol. The highest projector potential has been incorporated into the local potential, and subtracted from the lower projector potentials. This reduces the projector expansion by one order. The scattering properties of the angular momentum channels up to the original highest projector remain unchanged. But beyond, there is a difference. Higher angular momentum channels than the maximum projector experience a simple $-z_{\text{eff}}/r$ potential in the original ECP, while in the present work the scattering potential is the same as for the highest projector of the original potential. The author expects that the effect of this modification is minor, as the scattering properties for valence shell electrons were not changed. Since relativistic effects are small for the light elements, all electron calculations are used up to Ca for standard ECP DMol calculations.

Alternatively, averaged relativistic pseudopotentials (AREP)¹³ can be used. Like the ECP, the AREP have been derived in the context of wave function methods. The AREP have been adopted without change for the present work. Pseudopotentials for DFT have been developed mostly with plane wave convergence properties in mind. This has led to “soft” pseudopotentials with usually minimized z_{eff} . Neither ECP or AREP have been adapted specifically for DFT. If we regard Hartree–Fock (HF) and wave function theory beyond as an implementation of the density functional, this becomes an issue of transferability of the pseudopotential from one functional to another. A similar issue exists also for using a pseudopotential optimized for DFT with another DFT.

Matrix elements for \mathbf{k} representations

To calculate the DFT Hamiltonian and overlap matrices for the \mathbf{k} representations in a lattice there are two basic approaches. In the first approach, the \mathbf{k} -dependent phase factors are done simultaneously with the calculation of the matrix elements:

$$h_{i,j,\mathbf{k}} = \sum_{\mathbf{L}} \exp(i\mathbf{L}\mathbf{K}) \langle \phi_i(\mathbf{r} - \mathbf{L} - \mathbf{r}_\alpha) | h | \phi_j(\mathbf{r} - \mathbf{r}_\beta) \rangle. \quad (3)$$

\mathbf{L} are the three indices for lattice summations. Obviously, this part of the calculation scales linearly with the number of \mathbf{k} points used in the Brillouin-zone integration. Alternatively, the nonvanishing matrix elements (finite range of ϕ) on the lattice can be calculated first and the sparse matrix,

$$h_{i,j,\mathbf{L}} = \langle \phi_i(\mathbf{r} - \mathbf{L} - \mathbf{r}_\alpha) | h | \phi_j(\mathbf{r} - \mathbf{r}_\beta) \rangle, \quad (4)$$

stored. The lattice summation for matrix $h_{i,j,\mathbf{k}}$ is calculated in a later step. For unit cells larger in diameter than twice the cutoff radius, matrices Eqs. (3) and (4) contain the same number of matrix elements and the same number of terms. For more than a single \mathbf{k} point, use of Eq. (4) is clearly advantageous. For a small unit cell, calculation of Eq. (4) is several times more time consuming than evaluation of Eq. (3) for a single \mathbf{k} point, especially so, the larger the cutoff radius is. Since accurate calculations for small unit cells involve several to many \mathbf{k} points, Eq. (4) often still is advantageous. For simplicity Eq. (4) is used in calculations containing other \mathbf{k} points than the Γ point.

In analogy to the procedure of Eq. (4), density matrices with \mathbf{L} subscript are generated from the \mathbf{k} -dependent eigenvectors for use in the calculation of the density in real space and the Pulay derivative terms.

The Brillouin-zone integrations over all occupied orbitals are done basically with equispaced Fourier meshes similar to the ones proposed by Monkhorst and Pack.¹⁴ For a cell of insulating solid with \mathbf{k} space integration order of n_1, n_2, n_3 the “intensive” quantities (eigenvalues, etc.) calculated with the equiweight equispaced mesh of order n_1, n_2, n_3 must be the same as the ones for the supercell of size n_1, n_2, n_3 . This Gedanken experiment shows that the mesh spacing in reciprocal space is the basic variable governing convergence in insulators. By providing sufficient mesh resolution to resolve the band curvatures that can occur in practice, it is possible to design a mesh for insulators *a priori*.

As a default, meshes which contain the Γ point are used. Such meshes are guaranteed not to break the symmetry of the lattice. The default mesh is chosen as even order mesh with a \mathbf{k} -point spacing approximating a default target value,

$$n_i = 2N_{\text{int}} \left(\frac{|G_i|}{2d_k} \right), \quad i = 1, 2, 3, \quad (5)$$

where N_{int} denotes the nearest integer function, n_i is the mesh order along the reciprocal lattice vector G_i , and the resolution parameter $d_k = 0.03$ a.u. for default. Shifted meshes can be automatically generated and used too. If the usual translation into the first Brillouin zone is disregarded for the moment, the \mathbf{k} -vectors of the shifted mesh are $\mathbf{k} = \sum_{i=1}^3 \mathbf{G}_i(m_i - 1/2)/n_i$, where each m_i are numbers running from 0 to $n_i - 1$.

The Γ -point approximation remains the fastest method for diagonalization with larger cells, in particular when real diagonalizations are used. The Γ -point method is obtained by the default if all lattice parameters exceed 1.76 nm.

Symmetry can be used to avoid calculations at redundant \mathbf{k} points. This results then in a special \mathbf{k} -points method.¹⁴ Automatic space group symmetry recognition is done based on the atomic positions in the cell and the corresponding

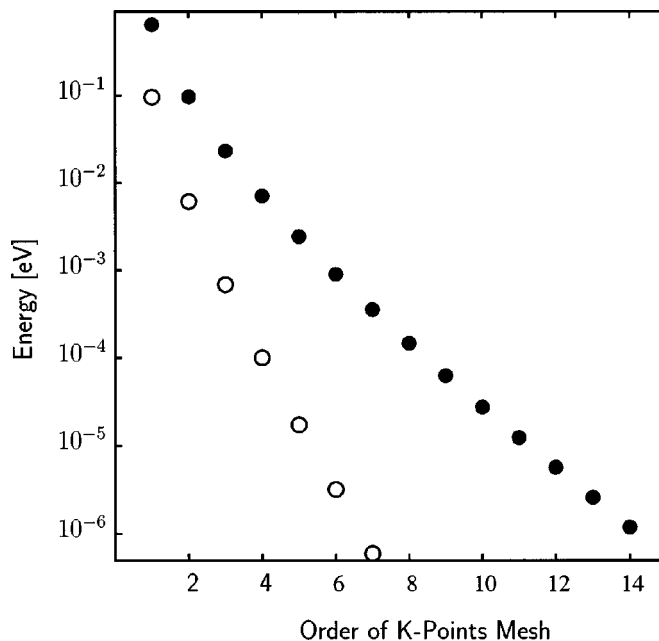


FIG. 1. Convergence of total energy for Si primitive cell with order of reciprocal space mesh. Full dots: meshes that contain Γ -point; empty dots: shifted meshes (1 Ha=27.2113961 eV).

lattice translations. The current method assumes standard orientation of the lattice. Furthermore, symmetry breaking, which may result from the start spin densities used to start up calculations of magnetic structures, are also taken into account. Automatic selection of a symmetry unique \mathbf{k} -point set is part of the present approach. In passing, it should be noted that using symmetry unique \mathbf{k} -points requires symmetrization of the density, etc. This is done by symmetrizing the population matrices mentioned before.

Figure 1 shows convergence with mesh size in the case of the Si primitive cell. Such exponential convergence is characteristic for insulators. The same levels of convergence map onto lower-order meshes, but with the same mesh spacing, for supercells. The default mesh is the order 6-mesh in the case of the Si primitive cell. The superior efficiency of the higher-order shifted meshes is put in a different and slightly less favorable perspective by considering the associated special (or symmetry unique) \mathbf{k} -points: the unshifted mesh of order 14 has 104 special points and the shifted mesh of order 10 has 110 points.

Brillouin-zone integrations for metals are complicated by the presence of the Fermi surface, which divides occupied and unoccupied orbitals in \mathbf{k} -space for the partially filled bands. Such integrations can be done by dividing up space into tetrahedra, within which band energies and matrix elements are linearized. Following Blochl,¹⁵ the tetrahedra are spanned on the full equidistant mesh. Symmetry is used again to identify the symmetry unique tetrahedra. As default, the second-order (Fermi surface curvature) corrections¹⁵ are applied. A consequence of the second-order correction is the appearance of negative integration weights at some \mathbf{k} -points for a fractionally occupied band. Writing the integration weight at a \mathbf{k} -point as a product of a Fourier-mesh weight and a band occupation leads to the appearance of negative

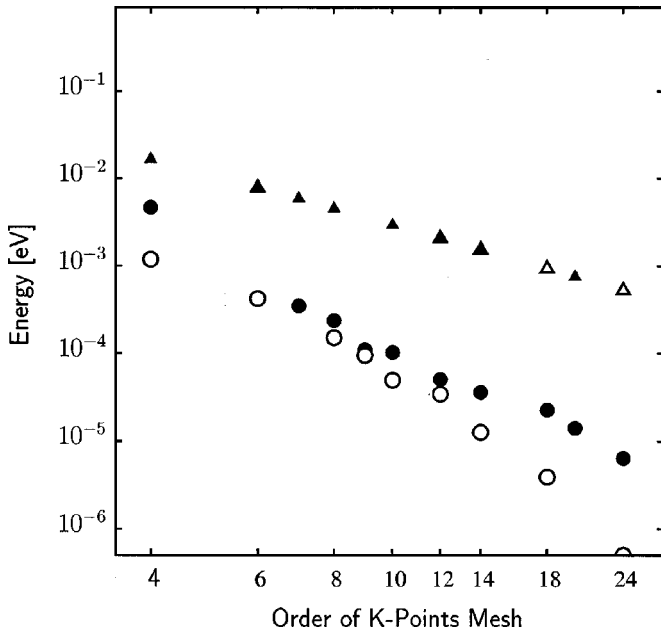


FIG. 2. Convergence of total energy for Cu primitive cell with order of reciprocal space mesh. Full symbols: meshes that contain Γ -point; empty symbols: shifted meshes; dots: tetrahedra with Bloechl corrections; triangles: linear tetrahedron method.

band occupation numbers at some \mathbf{k} -points. The integral band occupation remains positive definite. Applied to an insulating crystal this tetrahedron method gives identical special points, weights, and fast convergence as the Fourier mesh method when applied to insulators.

Figure 2 shows convergence with mesh size for copper metal. A power law is characteristic for integrations involving a Fermi surface. The improvement of accuracy obtained with the Bloechl curvature corrections is very significant. The default mesh for the Cu primitive cell is the mesh of order 8.

It may happen that an occupied or fractionally occupied band becomes degenerate with an unoccupied band at some \mathbf{k} -point. As a consequence the density associated with either of the orbitals becomes ill-defined. Since the total density of both orbitals is well-defined, we choose to populate both orbitals equally at that \mathbf{k} -point to avoid generating spurious oscillations in the SCF process. In metals it is found sometimes that a finer \mathbf{k} -mesh will not produce spurious oscillations while a more coarse \mathbf{k} -mesh does. Spurious SCF oscillations may alternatively be damped by finite temperature occupation or by Gaussian level broadening.

The scaling of the present method with respect to system-dependent physical and computational parameters is discussed now. The computation time T of matrix elements, density, and orbital derivative terms scales linearly with system size N . This is also true with a small caveat for the electrostatics.² The atom cutoff radius r_c impacts with a power of $2d$ asymptotically, where d is the dimensionality of the lattice. The diagonalization part goes with the third power of the system size and is linear in the number of \mathbf{k} -points used:

$$T \approx aNr_c^{2d}/M + bN^3(K/M)_{\text{int}} + cN \log M, \quad (6)$$

where a, b, c are machine and system-dependent parameters. The linear scaling part can be and has been made running on parallel machines with excellent load balancing. M is the number of parallel machines. Diagonalizations with multiple \mathbf{k} -points are distributed over the parallel processors; $(K/M)_{\text{int}}$ means that K/M must be rounded up to the next integer if K is not an integer multiple of M . Parallel processing entails communication overheads which scale logarithmically on a switched network. This and the granularity of the \mathbf{k} -points set a limit to the maximum number of parallel processors that is useful in the present implementation.

Gradient functionals

The method is currently set up to handle local spin density functional, and functionals with an explicit gradient dependence in addition. Density, and gradients if necessary, are calculated on the full numerical integration mesh. If the functional is written as

$$E_{\text{xc}}[\rho_\alpha, \rho_\beta, \nabla \rho_\alpha, \nabla \rho_\beta] = \int_{\text{num}} f_{\text{xc}}(\rho_\alpha, \rho_\beta, \gamma_{\alpha\alpha}, \gamma_{\alpha\beta}, \gamma_{\beta\beta}) d^3r, \quad (7)$$

where \int_{num} is a numerically evaluated integral, ρ_α, ρ_β are the up and down spin densities, and $\gamma_{\alpha\beta} = \nabla \rho_\alpha \nabla \rho_\beta$. The variational derivative of E_{xc} leads to matrix elements¹⁶

$$\langle \phi_i | \hat{\mu} | \phi_j \rangle_\alpha = \left\langle \frac{\partial f}{\partial \rho_\alpha} \phi_i \phi_j + \left(2 \frac{\partial f}{\partial \gamma_{\alpha\alpha}} \nabla \rho_\alpha + \frac{\partial f}{\partial \gamma_{\alpha\beta}} \nabla \rho_\beta \right) \nabla (\phi_i \phi_j) \right\rangle. \quad (8)$$

This approach does not need an analytical variational derivative of E_{xc} . However, in generating problem-adapted atomic basis sets by solving a radial differential equation for a spherical atom with that particular functional, it is expedient to use the variational derivative of E_{xc} , which yields a local potential $\mu(r)$. Rather than deducing the analytical variational derivative, one may use for the spherical atom case,

$$\mu_\alpha(r) = \frac{\partial f}{\partial \rho_\alpha} - \left(3 + r \frac{d}{dr} \right) \left(\frac{2}{r} \frac{\partial f}{\partial \gamma_{\alpha\alpha}} \frac{d\rho_\alpha}{dr} + \frac{1}{r} \frac{\partial f}{\partial \gamma_{\alpha\beta}} \frac{d\rho_\beta}{dr} \right). \quad (9)$$

Normally, it is preferred in the present approach to actually generate basis functions which are an exact solution of the spherical atom problem for the functional under consideration. For some recent functionals it has been found, however, that the variations of $\mu_\alpha(r)$ turn out to be large for certain atoms and lead to very high Fourier components in the basis functions. Such kink-like features of the partial waves make the molecular 3D integrations much slower converging. For the very fine atomic radial mesh this is no problem. Realizing, that such functionals have been tested out with Gaussian basis functions, it appears reasonable to use basis functions from a functional which generates smooth partial waves.

The B88PW91 or short BP functional combines Becke's 1988 exchange 17 with Perdew–Wang correlation 18. Like

TABLE I. Calculated properties for Cu vs. cutoff radius $R_c[a_0]$ using PWC local functional, tetrahedra with Bloechl corrections on shifted k -mesh $12 \times 12 \times 12$. For comparison calculations 11-d: all defaults, ($R_c = 11$ a.u., unshifted k -mesh $6 \times 6 \times 6$), 10-e: with pseudopotential (Ref. 35), BP: with BP functional (Refs. 17, 19), BP-e with BP functional and pseudopotential. E_t total energy shifted by 1637.938 Ha, E_s total energy with respect to spherical atom with confinement radius R_c .

Property vs R_c	8	10	12	14	11-d	10-e	BP	BP-e
E_t (mHa)	0.7	0.5	0.5	0.5	0.7
E_s (mHa)	160	158	158	158	158	161	113	113
$N(E_F)$ (eV $^{-1}$)	0.30	0.30	0.30	0.30	0.29	0.30	0.30	0.30
α (%)	-1.66	-1.54	-1.50	-1.51	-1.48	-3.67	+1.90	+0.14
B (GPa)	153	174	173	175	174	178	113	110

most other functionals, it generates sufficiently smooth partial waves. However, in its original formulation, numerical underflow hampers evaluation at low densities. Perhaps the most prominent underflow problem comes from the local part of the correlation functional. Perdew–Wang 19 (PWC) have defined

$$q_1(r_s) = 2p_1(p_3r_s^{1/2} + p_4r_s + p_5r_s^{3/2} + p_6r_s^2), \quad (10)$$

and

$$q_2(r_s) = \log(1 + 1/q_1(r_s)), \quad (11)$$

where $r_s = (3/4\pi\rho)^{1/3}$. The function $q_2(r_s)$ enters the gradient dependent part. In order to get improved accuracy for q_2 at small density the modified expression,

$$q_2(r_s) = \min\left(\frac{1}{q_1(r_s)}, \max\left(\log\left(1 + \frac{1}{q_1(r_s)}\right), \frac{1}{q_1(r_s)}\left(1 - \frac{1}{2q_1(r_s)}\right)\right)\right), \quad (12)$$

has been inserted. Some more modifications along these lines have been made.

RESULTS AND DISCUSSION

The convergence of the Cu crystal total energy with respect to the local basis cutoff R_c can be seen from Table I. Already for a cutoff radius of 10 a.u. (≈ 5.3 Å) the total energy appears to be converged to about 10 μ Ha. The bonding energy with respect to the atom is affected more by small cutoff radii, because the same cutoff radius was used confining the “free” atom. The calculated equilibrium lattice constant is fixed within 0.1% for $R_c > 9$ a.u. The bulk modulus calculated by the three point difference scheme from total energy has a numerical uncertainty of order 1–2 GPa. It is interesting to put these results in perspective with other calculations. A calculation using defaults gives essentially an identical result as the $R_c > 9$ a.u. results. The somewhat too short lattice constant is primarily a property of the PWC density functional. It is consistent with the too short lattice constant that the calculated bulk modulus is higher than the experimental value 137 GPa. The ECP, which was designed from first principles for Hartree–Fock (HF)-based calculations, gives results in fair agreement. However, the 2% smaller lattice constant as compared to the all electron calculation should be noted. This change of the energy surface is due to the modification of the atomic scattering properties

by the specific pseudopotential. It was found that the AREP,²⁰ which also was developed for HF-based calculations leads to a very similar extra lattice contraction for Cu.

Since the ECP incorporates scalar relativistic effects on bonding, one may ask if this contraction is a genuine relativistic effect or should be attributed to shortcomings of the pseudopotential. To sort this out, further calculations were done with $R_c = 10$ a.u. cutoff. With the all-electron scalar relativistic corrections a 2.30% shortened lattice constant was found, indicating a relativistic contraction for bulk Cu of 0.76%. The Stuttgart group also has a nonrelativistic version of their ECP; this yields -2.73%, or a relativistic contraction of 0.94%. Such a relativistic contraction is indeed particularly pronounced for group IB elements,²¹ e.g., for Cu₂ contractions from 2 to 6 pm are reported in Ref. 21. A contraction by 2 pm for the longer Cu–Cu bond in the bulk corresponds to 0.8% contraction of the lattice constant. While now 0.76%–0.94% contractions are attributed to a relativistic effect, the remainder about 1.2% has to be attributed to lack of portability and other deficiencies of the ECP and AREP when used with DFT.

Use of a gradient functional (BP) leads to a reduction of binding energy, a lattice expansion of order 2%, and a decrease of the bulk modulus below the observed value. This effect is consistent with the trend generally observed on going from local density approximation (LDA) to gradient dependent functionals.

The results of calculations for the Si crystal as a function of computational parameters are put together in Table II. The

TABLE II. Calculated properties of Si vs. cutoff radius $R_c[a_0]$ using HL-JMW local functional, DNP basis includes f -polarization function for Si, shifted k -mesh $8 \times 8 \times 8$. For comparison calculations 11-d: except for JMW all defaults: ($R_c = 11$ a.u., DND basis set, unshifted k -mesh $6 \times 6 \times 6$), 10-g: basis set including a g -polarization function, FLAPW (Ref. 36), and Ref. 22,^a 10-BP: with BP functional (Refs. 17, 19). E_t total energy per cell shifted by 576.82 Ha, E_s total energy per atom with respect to spherical atom with confinement radius R_c . $B_{\text{exp}} = 98.8$ GPa.

Property vs. R_c	8	10	12	11-d	10-g	FLAPW	10-BP
E_t (mHa)	4.5	3.3	3.3	-0.280	4.0	3.3 ^a	2 Ha
E_s (mHa)	194	191	191	189	192	...	163
E_g (eV)	0.52	0.53	0.53	0.59	0.50	0.50 ^a	0.67
α (%)	-0.54	-0.53	-0.56	-0.38	-0.45	-0.48	0.80
B (GPa)	108	96	97	96	95	97	90

^aReference 22.

TABLE III. Calculated zero point vibrational energy per atom and thermal corrections from Γ -point phonon frequencies in silicon supercell, energies in kcal/mol.

Cell size (atoms)	$E_{\text{vib}}(0)$	H(298)–H(0)
2	1.10	0.20
8	1.35	0.62
16	1.38	0.71
32	1.40	0.73
64	1.41	0.78

calculated values for cutoff radius 8, 10, and $12a_0$ use an extended basis set which includes an f -polarization function in the case of Si. It has been noted that the default DND basis set, which includes a d -polarization function for Si, misses up to about 1 kcal/mol per bond for tetrahedrally bonded silicon in compounds like in SiF_4 and the Si crystal. This is also the major reason for the difference with respect to the default calculation. With the extended basis set, electrostatics was calculated using up to hexadecapole moments, and the “xfine” mesh was used. Higher l polarization functions and higher multipole moments reduce the calculated value of the Kohn–Sham energy gap. Using g -polarization functions in addition further lowers the gap to near its converged value. This converged value is also obtained from high quality FLAPW calculations.²² (For precise comparison with FLAPW results the Hedin Lundqvist–Janak Moruzzi Williams functional is used, difference with PWC is minor for bulk Si.) It is well-known that the Kohn–Sham (KS) energy gap for most semiconductors is significantly smaller than the optical gap. It is gratifying to see that two different all electron implementations of DFT like DMol³ and FLAPW come to agree to within a fraction of a mHartree for energies, 0.1% for lattice constants, and 3% for the bulk modulus, when using the same density functional. The agreement with experiment is by no means as good as the different density functional results among themselves. The results are put in perspective by using a very well tested functional involving density gradients explicitly. It is significant and typical for the present state of the art with “gradient” functionals, that the lattice constant is larger than measured experimentally and that the bulk modulus is softened. The gradient functional does not lead to much a larger KS bandgap. The KS eigenvalue gap remains very significantly below the optical gap.

Harmonic vibration frequencies in molecules and at the Γ -point in reciprocal space for solids are calculated by two-point numerical differentiation of forces. Symmetry is used to diminish the number of calculations. The zero-point vibrational energy and the thermal corrections in solids involve a Brillouin zone integration for the phonons. This integration can be approximated with increasing accuracy by Γ -point sums for increasingly large supercells. Table III shows the convergence properties in the case of Si. Particularly by sampling the acoustic phonons at Γ in a small cell leads to an underestimation of the zero-point vibrational energy. Already at modest cell size a sufficient level of precision is reached. In the case of thermal corrections, the Γ -point sum approximates the acoustic phonon density of states by a set

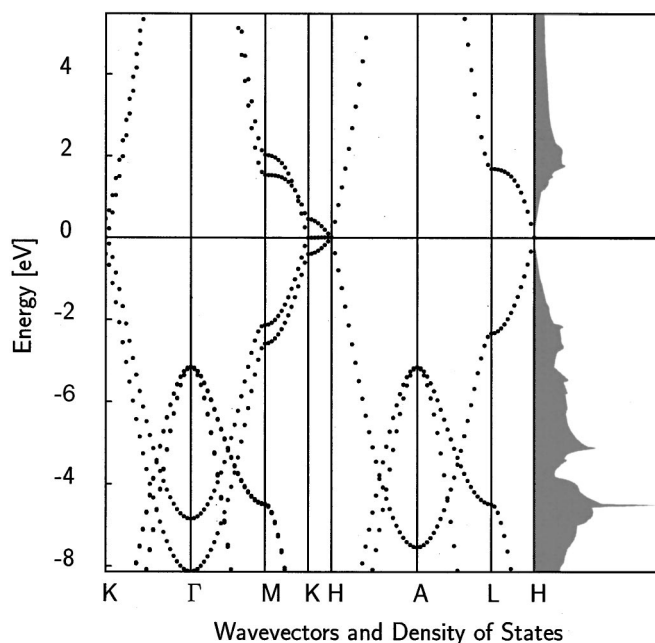


FIG. 3. Band structure and density of states for graphite.

of “Einstein model” discrete frequencies. Again it turns out that for the purpose of calculating enthalpies of formation accuracy on the order of 0.1 kcal/mol atom is obtained with cell size of 16 atoms.

The band structure and density of states of graphite are shown in Fig. 3. The bands become degenerate along the line K–H in the BZ, making graphite an example of a semimetal. The density of states has been calculated with the tetrahedron method using the unshifted $12 \times 12 \times 4$ mesh, the BP functional, and the experimental geometry ($a = 246$ pm, $c = 680$ pm) from the Cerius² database. For the k -mesh a multiple of 3 is required in the AB plane to actually have k -mesh points along the K–H line (Fig. 4). Since the degenerate bands at E_F can lead to the spurious occupation problem mentioned above, an $8 \times 8 \times 4$ k -mesh, which avoids such problems, was chosen for most of the calculations. The effect on calculated properties is minor except for optical properties. Using the PWC local functional, the lattice constant a

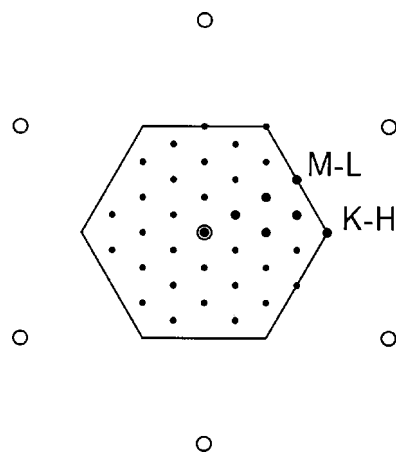


FIG. 4. Unshifted $6 \times 6 \times n$ mesh for hexagonal solid, projected onto ab plane. Special points are shown bold; circles: reciprocal lattice points.

TABLE IV. Calculated binding energies E_s (Ha) per atom for graphite and diamond at the experimental lattice constant for the PWC and the BP functional.

	E_{0v}	E_s PWC	E_s BP
Graphite	0.0062	0.3260	0.2824
Diamond	0.0065	0.3275	0.2782
ΔE		-0.0012	+0.0039

=244.7 pm and $c/a=2.694$ is found, while experiment is at $a=246.4$ or 247 pm and $c/a=2.724$ or 2.806 according to Refs. 23, 24. The best available experimental results involve thus an uncertainty of about 3% for the c -lattice parameter. The calculated bulk modulus is 297 GPa. Gradient-dependent functionals remove some or all of the overbinding found with local functionals. With the GGA functional^{25,26,19} $a=246.5$ pm and a 13.8% enlarged c/a ratio is found. The PBE functional²⁷ yields $a=247.0$ and 14.5% larger c/a as compared to experiment. The B88PW91 functional yields $a=246.7$ pm and an about 25% enlarged c/a ratio. The striking enhancement of the calculated c -lattice parameter involves only a small energy lowering of the total energy by about 1 mHa with respect to the experimental geometry. The weak graphite interlayer interaction makes the calculated c -parameter very sensitive to the choice of basis set. Better basis sets tend to make calculated c larger. The present result is in contradiction with the GGA result from Ref. 28. However, the author is confident that qualitative confirmations of the present result could be found in a number of waste-paper baskets already. While the present result is not documented in the literature yet, it is not a complete surprise. It is known that gradient dependent functionals lead to dramatic weakening of weak bonds. In particular, the B88 exchange part of the functional, which is known to greatly improve calculated dissociation energies of molecules, has been known for making certain weak bonds turn out unbound.^{29,30} Despite that weakly bonded systems have been considered by design for the very recent HCTH-147 functional,³¹ it nevertheless overestimates graphite c/a by $\approx 20\%$. It is interesting to compare total energies of graphite and diamond, Table IV. The zero-point vibration energy of graphite was calculated with 16 and 36 atom supercells, the one for diamond with a 16 atom supercell. Vibrational calculations were done at the experimental lattice parameters using the PWC functional. The present calculations with the PWC functional yield diamond to be more stable by 1.2 mHa per atom (32 meV or 0.7 kcal/mol). The slightly larger zero point vibration energy of diamond is not sufficient to revert this ordering³² in the present calculation. With the BP functional graphite is more stable by 3.9 mHa (106 meV or 2.4 kcal/mol).

Starting from the experimental structure of orthorhombic sulfur α -S₈,³³ which is the thermodynamic reference state for S at low temperature, geometry optimizations for fixed lattice constants were done with the BP functional. Displacements with respect to the experimental geometry remained all below 1 pm. Lattice vibrations were calculated as Γ -point vibrations of the primitive cell consisting of 32 sulfur atoms.

The formation energy of the gas phase atom (with re-

TABLE V. Deviations from experimental enthalpies of formation [kcal/mol] at 298 K for G2 neutral molecule set: (a) For energy, geometry and frequencies: functional B88PW91, basis DNP, frequencies scaled 0.98. (b) Energy: functional B88PW91, basis DNP, geometry MP2, frequencies: HF scaled 0.86, all energies in kcal/mol. (c) Same as (a) but using calculated atomic enthalpies for formation from molecular reference states H, N, O, F, Cl, and Solids C, Si, S. (d) Same as (c) but experimental atom formation energy used for F. (e) same as (a) using PBE functional. (f) PBE functional, using calculated atomic enthalpies for formation from molecular reference states H, N, O, F, Cl, and solids C, Si, S.

	Number	Mean	rms	Avg abs	Min	Max	Min at	Max at
(a)								
G2-1	55	0.2	5.8	4.6	-13.8	14.6	Si ₂ H ₆	O ₂
G2-2	93	2.2	9.0	6.7	-12.5	25.2	SiF ₄	NO ₂
All	148	1.5	8.0	5.9				
(b)								
G2-1	55	0.0	5.6	4.5	-13.2	13.9	Si ₂ H ₆	O ₂
G2-2	93	1.5	8.7	6.5	-12.6	24.7	SiF ₄	NO ₂
All	148	1.0	7.7	5.8				
(c)								
G2-1	55	-0.3	4.5	3.5	-10.3	9.4	LiF	S ₂
G2-2	93	3.0	9.4	7.4	-31.4	18.3	SiF ₄	pyridine
All	148	1.8	7.9	6.0				
(d)								
G2-1	55	0.1	4.5	3.6	-9.7	9.7	OH	F ₂
G2-2	93	5.1	8.7	7.2	-15.5	23.6	SiCl ₄	ClF ₅
All	148	3.2	7.4	5.9				
(e)								
G2-1	55	4.1	8.1	6.3	-9.0	21.0	Si ₂ H ₆	CO ₂
G2-2	93	15.8	18.8	16.1	-5.2	37.8	CH ₃ SiH ₃	pyridine
All	148	11.5	15.7	12.4				
(f)								
G2-1	55	1.1	5.9	4.6	-10.4	14.2	OH	Si ₂ H ₆
G2-2	93	5.4	10.2	8.6	-23.2	19.8	SiF ₄	pyridine
All	148	3.8	8.9	7.1				

spect to the reference state) is an important intermediate quantity in a theoretical discussion of molecular enthalpies of formation. In previous discussions of molecular enthalpies of formation experimental values were used for the atom enthalpies.

For the discussion of bonding energetics the B88PW91 functional is used.^{17,25} According to Curtiss *et al.*³⁴ this functional produces 7.85 kcal/mol average absolute deviations from well-established experimental enthalpies of formation ($\Delta_f H^0$) at 298.15 K for their G2 test set consisting of 148 neutral molecules. The performance for that test obtained with the present approach is summarized in Table V. Test 4(B) uses MP2 geometries and scaled HF frequencies.³⁴ Tests 4(A) and 4(B) are almost identical. The slightly off minimum geometries in 4(B) reduce the small mean overbinding of 4(A) leading to a superficially improved result.

Table VI shows the enthalpy of formation for free atoms in their Hund's rule ground state. E_b is the binding energy of the reference state with respect to the spin-unrestricted spherical atom. The spherical DFT atom energy serves merely as an easily accessible reference number, since spherical atoms are used to construct the variational basis.

TABLE VI. Calculated enthalpies of formation [kcal/mol] at 298 K for C, Si, and S gaseous atoms from their respective reference state. Calculations using BP functional, reference state (solid) with experimental geometry. E_s denotes the calculated binding energy of the reference state with respect to spin-unrestricted spherical atoms. E_{ns} is the calculated Hunds-rule energy gain with respect to spin-unrestricted spherical atom. E_{0v} is the zero-point vibrational energy calculated from 36, 64, and 32 atom cells, respectively. E_{th} thermal correction.

		Graphite	Silicon	α -S ₈
E_s	(+)	177.18	102.89	66.76
E_{ns}	(+)	-3.42	-1.12	-4.42
E_{0v}	(-)	3.88	1.41	0.96
E_{th}	(-)	0.25	0.78	1.05
Calc.	$\Delta H_f(298)$	169.63	99.58	60.33
Exp.	$\Delta H_f(298)$	169.98	106.6	65.66

The atom calculation for the Hund's rule ground state frequently involves nonspherical densities. This is handled as a single atom calculation in the molecular framework. The Hund's rule level occupations are chosen to maximize S_z , which formally implies a single determinant wave function. The nonspherical spin densities of the Hund's rule atom lead to an atomic ground state energy lower by several kcal/mol than the one from our spin-unrestricted spherical atom.

It is apparent that the enthalpy of formation for Si and S is underestimated. This is true for the BP functional. For the PWC local functional the underestimate turns again into an overestimate. Intermediate results in appealing agreement with experiment for the solids are obtained from functionals like GGA or PBE²⁷ which have a smaller enhancement factor $f(s)$ for exchange in the limit of large scaled gradient s . Unfortunately GGA or PBE have much inferior results compared to BP when tested with the G2 neutral molecule enthalpies of formation. On the other hand the enthalpies of formation for the atoms from the solid reference state remain in the range of expectations from G2 with the BP functional, i.e., on the order of 6 kcal/mol average deviation. One may use the calculated enthalpies of formation for the elements H, N, O, F, and Cl from the diatomic reference states and for C, Si, and S from the solid calculations instead of potentially less consistent, experimentally deduced values. C, Si, and S are the most frequently used solid state reference states for the G2 test set. Next in importance is white phosphorus. Unfortunately this solid is crystallographically not well defined. Therefore calculation of solid reference states for P and the less important Li, Be, B, Na, Al is disregarded for this work. As it turns out, using calculated reference states deteriorates the BP-G2 performance Table V (C). Especially the spread for the G2-2 subset increases unfavorably. This is mainly due to using the atom formation enthalpy from the F₂ molecule. This reference state happens to be maximum deviation for the G2-1 subset Table V (A) and (B). Without fluorine, indeed, there is an improvement seen in the rms deviations, (D). Whether or not calculated reference states are used, the BP functional yields an average deviation of 6 kcal/mol, and maximum deviations exceeding 20 kcal/mol for the G2 test set. This appears to be the present state of the art obtainable

with functionals that have only explicit dependence on density and density gradients.

The performance of the PBE functional²⁷ using experimental atomic enthalpies of formation is impaired by overestimation of the atomic dissociation energy, Table V (E). When calculated atomic enthalpies of formation are used, Table V (F) results. This is very close in performance to the one by BP. The ability of the PBE functional to describe differences in bonding among various compounds is very similar to BP, which remains the most performant-purely-density plus gradient-dependent functional for the present test.

CONCLUSIONS

Recent extensions of the DMol³ density functional method are described. This method is designed to do electronic structure calculations for local and gradient-dependent functionals. It uses numerical solutions of DFT-free atoms as part of its basis set, and thus gives highly accurate DFT solutions for the separated atoms limit. Typically a doubled numerical basis set with d -polarization functions (DND) is used for molecular and solids calculations. Basis sets with shorter tails than previously useable significantly speed up calculations for large molecules and solids. Semilocal pseudopotentials help both to introduce scalar relativistic effects and to speed up calculations. The extension with Brillouin zone integrations is specific for calculations with periodic boundary conditions. The tetrahedron method for Brillouin zone integration deals with the complication arising from the Fermi surface in metals; it is designed to become a spectral method with exponential convergence in the case of semiconductors and insulating compounds. The method is used here for solid state calculations of semiconductor Si and insulator α Sulfur, the semimetal graphite, and metallic Cu. An upshot of these benchmark calculations is that the larger part of uncertainty in the results is due to limitations in the presently available functionals, and not with limitations of the present method of calculation.

Si, S, and graphite are also standard thermodynamic reference states. These were used together with the molecular reference states for H, N, O, F, Cl to reassess the performance of two gradient dependent density functionals for the G2 neutral test set. If experimental atom formation energies are used together with calculated molecular dissociation energies to define the calculated molecular enthalpies of formation, B88P91 turns out as the best performing functional for DMol. While B88P91 performance remains virtually unchanged when using the calculated atom formation energies, it is found that the performance of the PBE functional is much improved, coming close to the B88P91 performance. It is expected that the present method will prove useful and efficient in finding density functional results for molecules, solids, and in particular, surfaces with molecules.

ACKNOWLEDGMENTS

The author thanks A. Chaka and G. Fitzgerald for careful reading and constructive criticism of the manuscript. Stimulating discussions with J. Andzelm are gratefully acknowledged.

- ¹B. Delley, J. Chem. Phys. **92**, 508 (1990).
- ²B. Delley, J. Phys. Chem. **100**, 6107 (1996).
- ³B. Delley, D. Ellis, A. Freeman, E. Baerends, and D. Post, Phys. Rev. B **27**, 2132 (1983).
- ⁴J. Harris, Phys. Rev. B **31**, 1770 (1985).
- ⁵J. W. Andzelm, C. Kölmel, and A. Klamt, J. Chem. Phys. **103**, 9312 (1995).
- ⁶B. Delley, J. Comput. Chem. **17**, 1152 (1996).
- ⁷B. Delley, Int. J. Quantum Chem. **69**, 423 (1998).
- ⁸O. F. Sankey and D. J. Niklevski, Phys. Rev. B **40**, 3979 (1989).
- ⁹L. Kleinman and D. M. Bylander, Phys. Rev. Lett. **48**, 1494 (1982).
- ¹⁰X. Gonze, R. Stumpf, and M. Scheffler, Phys. Rev. B **44**, 8503 (1991).
- ¹¹M. Dolg, U. Wedig, H. Stoll, and H. Preuss, J. Chem. Phys. **86**, 866 (1987).
- ¹²A. Bergner, M. Dolg, W. Kuechle, H. Stoll, and H. Preuss, Mol. Phys. **80**, 1431 (1993).
- ¹³L. F. Pacios and P. A. Christiansen, J. Chem. Phys. **82**, 2664 (1985).
- ¹⁴H. J. Monkhorst and J. D. Pack, Phys. Rev. B **13**, 5188 (1976).
- ¹⁵P. E. Bloechl, Phys. Rev. B **49**, 16223 (1994).
- ¹⁶J. A. Pople, P. M. W. Gill, and B. G. Johnson, Chem. Phys. Lett. **199**, 557 (1992).
- ¹⁷A. D. Becke, Phys. Rev. A **38**, 3098 (1988).
- ¹⁸J. P. Perdew, in *Electronic Structure of Solids '91*, edited by P. Ziesche and H. Eschrig (Akademie Verlag, Berlin, 1991).
- ¹⁹J. P. Perdew and Y. Wang, Phys. Rev. B **45**, 13244 (1992).
- ²⁰M. M. Hurley, L. F. Pacios, P. A. Christiansen, R. B. Ross, and W. C. Ermler, J. Chem. Phys. **84**, 6840 (1986).
- ²¹P. Pykkö, Chem. Rev. **88**, 563 (1988).
- ²²W. Wolf (personal communication).
- ²³P. Trucano and R. Chen, Nature (London) **258**, 136 (1975).
- ²⁴P. H. Gamlen and J. W. White, J. Chem. Soc., Faraday Trans. **72**, 446 (1976).
- ²⁵Y. Wang and J. P. Perdew, Phys. Rev. B **44**, 13298 (1991).
- ²⁶J. P. Perdew, Physica B **172**, 1 (1991).
- ²⁷J. P. Perdew, K. Burke, and M. Ernzerhof, Phys. Rev. Lett. **77**, 3865 (1996).
- ²⁸I.-H. Lee and R. M. Martin, Phys. Rev. B **56**, 7197 (1997).
- ²⁹B. Delley, in *Modern Density Functional Theory: A Tool for Chemistry*, edited by J. M. Seminario and P. Politzer, Theoretical and Computational Chemistry (Elsevier, Amsterdam, 1995), Vol. 2.
- ³⁰Y. Zhang, W. Pan, and W. Yang, J. Chem. Phys. **107**, 7921 (1997).
- ³¹A. D. Boese, N. L. Doltsinis, N. Handy, and M. Sprik, J. Chem. Phys. **112**, 1670 (2000).
- ³²M. T. Yin and M. L. Cohen, Phys. Rev. B **29**, 6996 (1984).
- ³³S. J. Rettig and J. Trotter, Acta Crystallogr., Sect. C: Cryst. Struct. Commun. **43**, 2260 (1987).
- ³⁴L. A. Curtiss, K. Raghavachari, P. C. Redfern, and J. A. Pople, J. Chem. Phys. **106**, 1063 (1997).
- ³⁵M. Dolg, U. Wedig, H. Stoll, and H. Preuss, J. Chem. Phys. **86**, 866 (1997).
- ³⁶A. Zupan, P. Blaha, K. H. Schwarz, and J. P. Perdew, Phys. Rev. B **58**, 11266 (1998).